IOPscience iopscience.iop.org

Home Search Collections Journals About Contact us My IOPscience

Wideband excitation of an electrostatic vibration energy harvester with power-extracting end-stops

This content has been downloaded from IOPscience. Please scroll down to see the full text.

2013 Smart Mater. Struct. 22 075020

(http://iopscience.iop.org/0964-1726/22/7/075020)

View the table of contents for this issue, or go to the journal homepage for more

Download details:

IP Address: 155.198.134.118
This content was downloaded on 22/10/2013 at 13:48

Please note that terms and conditions apply.

Smart Mater. Struct. **22** (2013) 075020 (9pp) doi:10.1088/0964-1726/22/7/075020

Wideband excitation of an electrostatic vibration energy harvester with power-extracting end-stops

Cuong Phu Le[1], Einar Halvorsen[1], Oddvar Søråsen[2] and Eric M Yeatman[3]

[1] Department of Micro and Nano Systems Technology, Vestfold University College, Horten, Norway
[2] Department of Informatics, University of Oslo, Oslo, Norway
[3] Department of Electrical and Electronic Engineering, Imperial College London, UK

E-mail: Einar.Halvorsen@hive.no

Received 18 February 2013, in final form 13 May 2013
Published 7 June 2013
Online at stacks.iop.org/SMS/22/075020

Abstract
An electrostatic energy harvester with two-stage transduction is investigated for enhancement of bandwidth and dynamic range. The harvester includes a primary proof mass with two main transducers and end-stops for the proof mass functioning as secondary transducers. In the small acceleration regime, the power is primarily obtained from the main transducers. In the high acceleration regime, the mass impacts the end-stops and actuates the secondary transducers, generating additional output power. The device is designed and fabricated using the SOIMUMPs process and has a total active area of 4×5 mm^2. Under wideband acceleration at high levels, the experimental results show that the total output power increases to about twice the output power of the main transducers, while the 3 dB-bandwidth is enlarged by a factor of 6.7 compared to the linear-response bandwidth at low levels. In comparison with a reference device made with the same die dimensions, the two-stage device improves output power instead of saturating when the maximum mass displacements of both devices reach the same limit. Measurement of output power demonstrates that the device with the transducing end-stops give an efficiency of 23.6%, while this value is 14.1% for the reference device with the conventional end-stops, at an acceleration spectral density of $S_a = 19.2 \times 10^{-3}$ g^2 Hz^{-1}. The efficiency is improved about by 9.5% in the impact regime.

(Some figures may appear in colour only in the online journal)

1. Introduction

Recent developments in microelectromechanical systems (MEMS) technology offer alternatives to using batteries in the autonomous operation of remote sensors or actuators. Energy harvesting from motion can supply electrical energy for the replacement of batteries or for extending system lifetime. A spring–mass system is typically used in energy harvesters for scavenging power from ambient vibration. Three common mechanisms for energy conversion applied for harvesting systems are electromagnetic, piezoelectric and electrostatic transduction [1–9]. In practical harvesters with high quality factors Q, the proof mass motion is restricted to avoid spring fracture under high acceleration, or simply due to the finite die dimensions. Several harvester prototypes have mechanical end-stops that enforce this restriction and also provide an increase of bandwidth [10–18]. Use of mechanical end-stops reveals a typical shortcoming that the output power saturates or has only a minor rise under large vibrations. This results from the proof mass reaching the maximum displacement amplitude when impacting the end-stops. Recent works have used macroscale piezoelectric energy harvesting devices to scavenge output power also from the impact mechanism [19–29].

Within the two-stage device principle, utilization of the secondary transducers as end-stops gave a demonstrated

 © 2013 IOP Publishing Ltd Printed in the UK & the USA

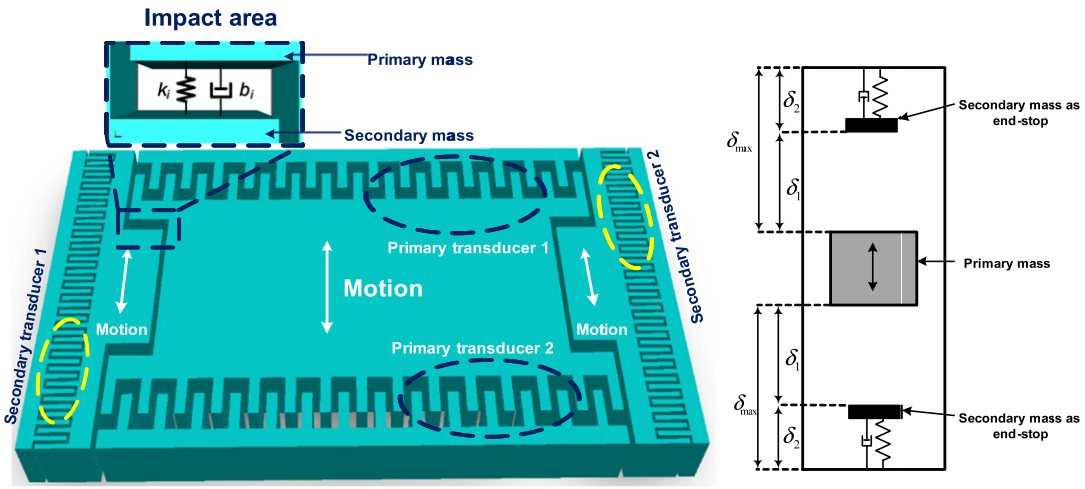

Figure 1. Main features of the two-stage electrostatic energy harvester.

improvement of output power and bandwidth under sinusoidal excitations in our own previous work [30]. By comparing to a reference device of the same die dimension and maximum displacement amplitude, the impact device gave a much higher output power. In this work, a harvester prototype is driven instead by wideband vibrations where the acceleration waveform is unpredictable in practice. Therefore, we expect no sharp transition to displacement limited operation with increasing vibrations, but rather a gradually more frequent and strong engagement of the end-stop transducers as the main proof mass is more frequently accelerated beyond the limit. Detailed characterization of the device concept shows that improved efficiency and bandwidth enhancement are achieved using additional transducing end-stops under wideband excitations.

2. MEMS design and device

In our two-stage impact device, the mechanical end-stops are provided by additional secondary transducing structures within the same die. The two transducer types have different functions in the compact MEMS device. At a low acceleration level, the primary proof mass displacement is less than the limit and almost no impact occurs. The output power of the energy harvesting device is mainly obtained from the primary one. However, a high acceleration level forces the main proof mass displacement to the limit, impacting the end-stops and activating the secondary transducers. Therefore, mechanical energy from the impacts is converted to electrical energy and adds to that from the primary transducers. As a result, the total output power of the device can be increased substantially under a high acceleration amplitude.

Figure 1 shows a schematic of the device design. The two-stage electrostatic design consists of two types of transducers: primary transducers and secondary transducers. The primary transducers, taking up the largest part of the area, are ordinary comb-drive capacitor structures connected to a proof mass suspended by four linear springs. They are overlap-varying anti-phase transducers. The primary proof mass displacement amplitude is limited to a total of $\delta_{max} = 10\ \mu$m. The active chip area is 4×5 mm^2. A smaller area is used for the secondary transducers, which have a higher stiffness and function as end-stops for the primary mass. The two secondary transducers are designed to limit motion of the primary mass in both directions of motion. Each secondary transducer has a gap-closing capacitor. The overall mechanical stiffness is made piece-wise linear by the contact between secondary and primary masses, which aids in increasing the system bandwidth [12]. The contact surfaces between the primary and secondary masses are shaped as half-cylindrical bumps contacting on flat surfaces. The distance between the primary and secondary masses at equilibrium is $\delta_1 = 6\ \mu$m. The primary mass hits the secondary masses when their relative displacement is beyond δ_1. The secondary displacement is limited to a maximum amplitude of $\delta_2 = 4\ \mu$m by conventional end-stops. Thus, the primary mass can be displaced to a maximum amplitude of $\delta_{max} = \delta_1 + \delta_2 = 10\ \mu$m during mutual interaction.

Figure 2 shows a close-up view of the spring design and the impact area in the fabricated device. The springs of both primary and secondary transducers are folded beams in order to achieve a mechanically linear characteristic. The secondary masses are much smaller than the primary mass. Therefore, the resonance frequency of the primary transducers is much lower than that of the secondary transducers. The primary and secondary masses are accelerated in the same direction. The device was fabricated in MEMSCAP's SOIMUMPS process, which is based on silicon micromachining of silicon-on-insulator wafers with a handle substrate thickness of 400 μm, a buried oxide layer with a thickness of 2 μm, a doped silicon layer as the device layer with a thickness of 25 μm and a 0.52 μm-thickness pad metal. The maximum aspect ratio of the device layer micromachining is 12.5. A cavity under the proof mass is released by deep reactive ion etch through the substrate. Further details of the process are given in [31]. The fundamental parameters of the design for the primary and secondary transducers are listed in table 1. Further details on the device design are found in [30].

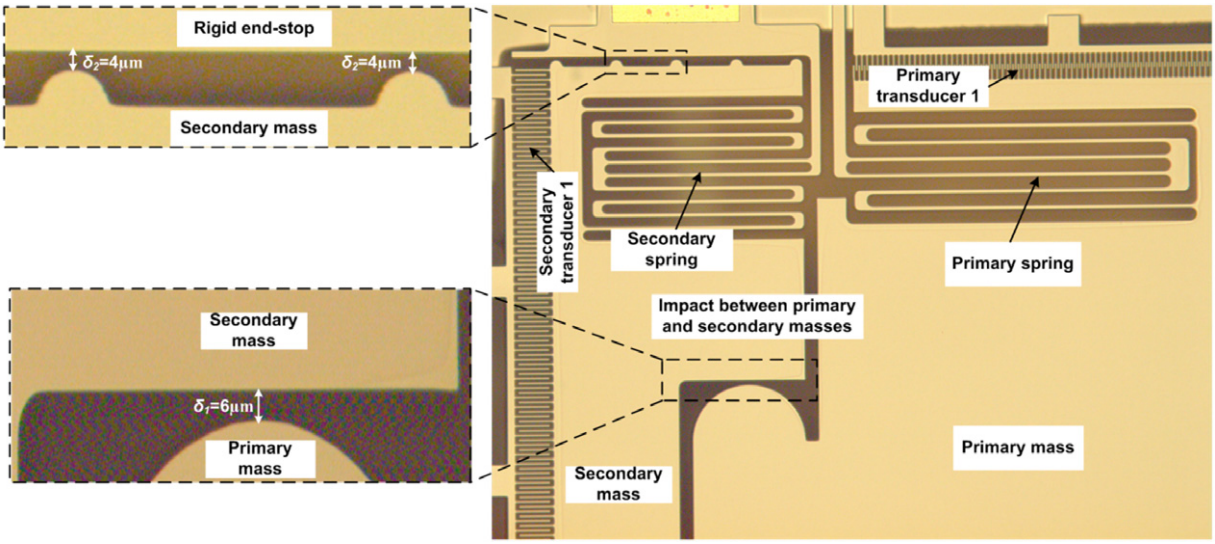

Figure 2. Close-up view of the spring design, the capacitor and the impact area in the fabricated device.

Table 1. Parameters of the primary and secondary transducers.

Parameters	Primary transducers	Secondary transducers 1 and 2
Finger length	25 μm	55 μm
Finger width	2 μm	2 μm
Nominal overlap	10 μm	50 μm
Nominal gap	2 μm	5 μm
Spring length	530 μm	335 μm
Spring width	6.2 μm	6.2 μm
Mass	1.10 mg	0.05 mg

3. Experimental results

The experimental setup is implemented by gluing the devices onto a printed circuit board, as shown in figure 3. The mechanical vibration source is a shaker system, including a vibratory exciter TIRA and its power amplifier. The output ports are connected to the load resistances R_L and amplifiers acting as buffers for data acquisition. The data from the input excitation signal and the output voltage are concurrently measured and analyzed using National Instruments' LabView program with an NI-USB-6211 DAQ at a sampling rate of 12 kHz. This instrument is also able to control the acceleration signal from the shaker system. The excitation signal is measured by an accelerometer from PCB Piezotronics Inc. model 352A56A.

3.1. Electrical characterization

An impedance characterization of a primary transducer was performed using the Precision Impedance Analyzer 4249A 40 Hz–110 MHz, Agilent Technologies. The impact device sample used here is a different sample from the same batch, but with the same design that we investigated for harmonic vibrations in [30]. The frequency was swept in the range from 600 to 700 Hz with input sources of 10 V DC and 0.5 V AC, connected to one port of the primary transducers.

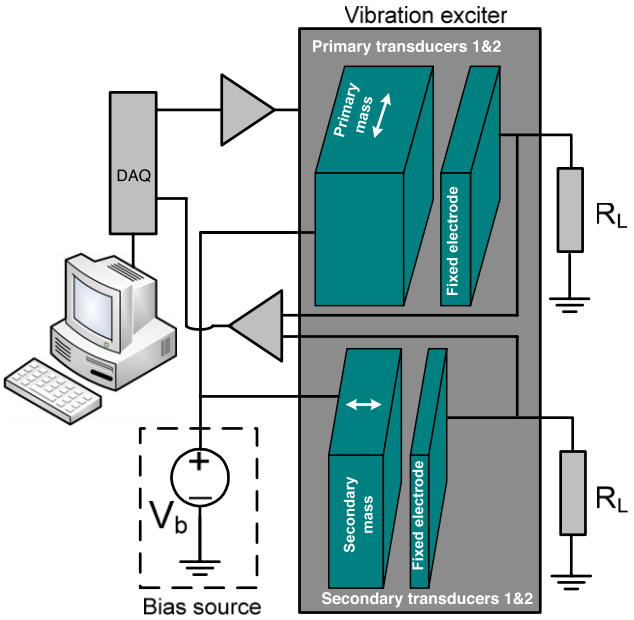

Figure 3. Sketch of the electrical setup for the two-stage electrostatic energy harvester.

The impedance analysis gives a lowest value of 21.5 MΩ, which was used for R_L in investigating the performance of the device in the narrowband regime [30]. The same value of R_L was then kept for evaluation of the output power with wideband vibrations in this paper. The theoretically optimal load resistance under wideband excitations is only about 21.2% larger in the absence of load parasitics. Parasitic capacitance due to the load in the measurement circuits further reduces the optimal value. All transducers of the device are connected to external loads with the same value R_L for simplicity and are biased at the same constant voltage V_b connected to the movable electrodes during operation. The following sections present experimental performance with a chosen bias value of $V_b = 12$ V. The effects of the bias on

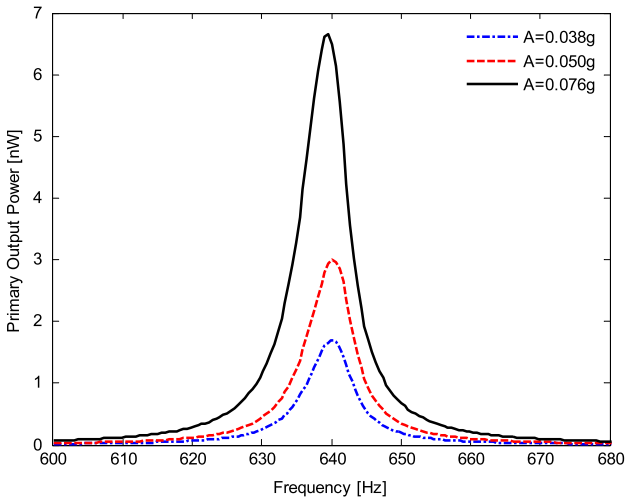

Figure 4. Measured output power of the primary transducers for different accelerations $A = 0.04g$, $0.05g$ and $0.08g$ at a bias voltage $V_b = 12$ V.

output power of the impact device are discussed in detail in section 4 when comparing to a reference device.

3.2. Sinusoidal excitations

The frequency response of the impact device under sinusoidal excitations is considered as a first experimental check. The frequency responses for various excitation levels are illustrated in figure 4 at a bias voltage $V_b = 12$ V. For low accelerations, the primary mass does not reach the secondary masses. The primary transducers then behave as ordinary comb-drive transducers in the linear regime and there is negligible output power from the secondary transducers. The output power is proportional to the squared acceleration amplitude A^2. For example, the measured output power increases from 1.68 to 6.65 nW when increasing A from 0.038 to 0.076 g at the resonance frequency.

3.3. Wideband excitations

Performance of the impact device is primarily characterized under random wideband excitations in order to observe the dynamic interplay between the primary and secondary transducers, and their achievable output powers. The wideband signals are characterized by their acceleration power spectral density (PSD), which is approximately constant below a chosen cut-off frequency of 10 kHz. The technique used to generate the wideband signals for the system was described in our previous work [18], which also shows an example spectrum. The chosen bandwidth of the excitation signal implies that the actual vibration bandwidth is limited by the shaker to 2 Hz–7 kHz. The acceleration PSDs are increased from low to high levels to reach interaction between the primary and secondary masses. The total output power of the impact device is evaluated as the sum of the primary and secondary outputs.

Figure 5 shows measured output voltages across the loads for the primary and secondary transducers at low and high

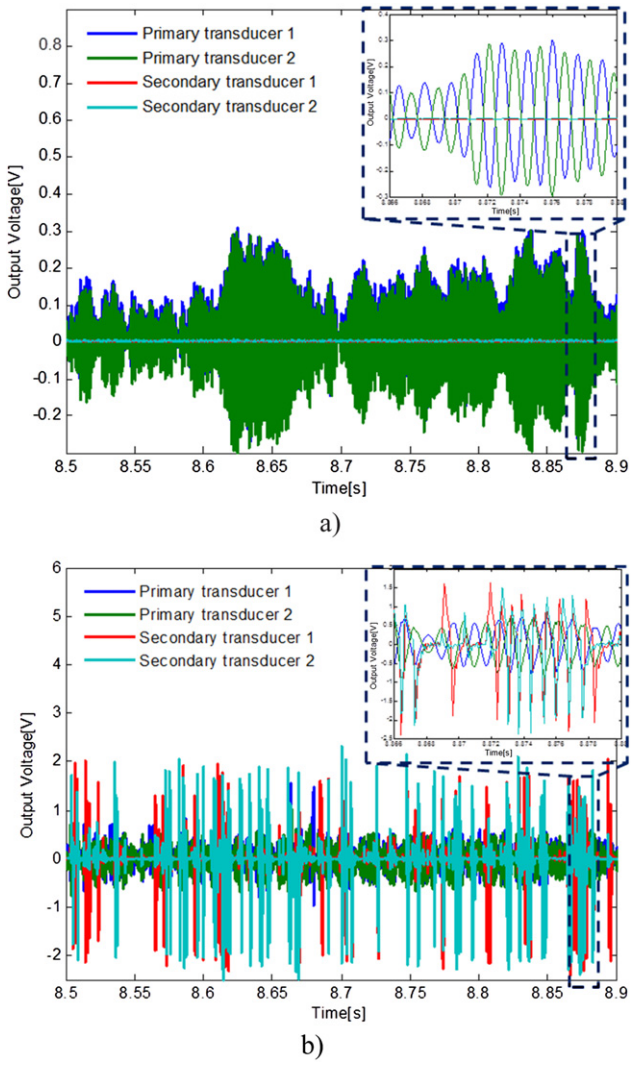

Figure 5. Measured output voltages of primary and secondary transducers for: (a) $S_a = 3.5 \times 10^{-5}$ g^2 Hz^{-1} and (b) $S_a = 16.7 \times 10^{-4}$ g^2 Hz^{-1} at a bias voltage $V_b = 12$ V.

acceleration levels at a constant bias voltage $V_b = 12$ V. A very small acceleration power spectral density (PSD) of $S_a = 3.5 \times 10^{-5}$ g^2 Hz^{-1} rarely causes the main mass to impact the secondary mechanisms, although some secondary outputs are seen due to direct excitation from the external vibration source. Therefore, the primary transducer outputs are dominant over the secondary transducer outputs, as observed in figure 5(a).

In figure 5(b), a high acceleration PSD of $S_a = 16.7 \times 10^{-4}$ g^2 Hz^{-1} gives frequent impacts between the primary and secondary masses. These internal impacts then become a major source of excitation of the two secondary transducers and their output voltages become substantial compared to the small acceleration PSD regime. The secondary mechanisms convert the excess kinetic energy of the primary mass to electrical energy through the action of the secondary springs and transducers, giving extra output power.

We can observe from figure 5(b) that the secondary transducers display somewhat dissimilar waveforms and that the dissimilarity is not entirely consistent over time, despite

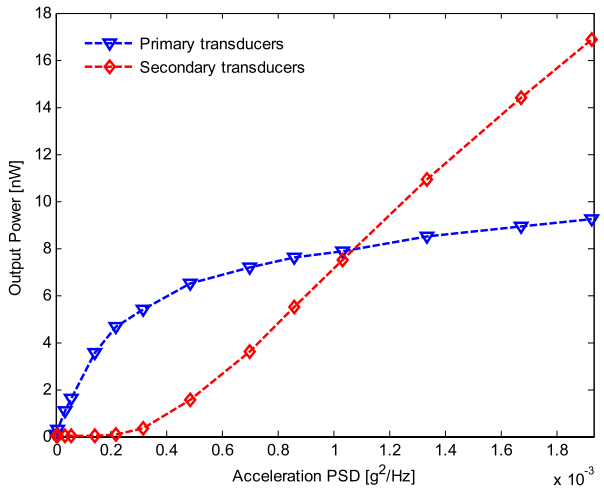

Figure 6. Measured output power of primary and of secondary transducers versus acceleration PSD at a bias voltage $V_b = 12$ V.

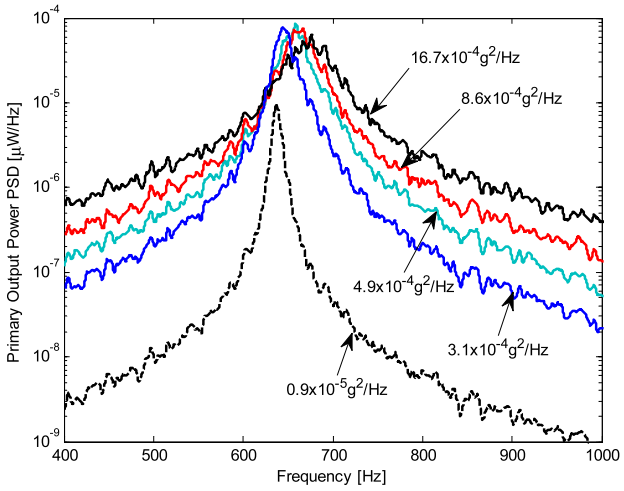

Figure 7. Measured PSDs of the primary outputs for acceleration PSDs: 0.9×10^{-5}, 3.1×10^{-4} , 4.9×10^{-4}, 8.6×10^{-4} and 16.7×10^{-4} g^2 Hz^{-1} as shown at a bias voltage $V_b = 12$ V.

their identical designs. This observation can be explained by slightly different spring stiffness, distance between the primary and secondary masses, and/or distance to the rigid end-stops in the fabricated device. Thus, the dynamic interplay between them leads to the dissimilarity of the outputs. This is supported by the slight differences in phase between the secondary transducer outputs observed in [30] with a harmonic excitation.

Figure 6 illustrates the dependence of the primary and secondary output powers on the acceleration PSDs. At low excitation, the primary output power is greater than that of the secondary output, which is extremely small. This is due to the rare impacts between primary and secondary transducers. Both output powers of the two transducers increase when further increasing the acceleration PSD. Around $S_a = 3.1 \times 10^{-4}$ g^2 Hz^{-1}, the internal impact becomes strong and results in recognizable secondary output power. The primary output power then grows at a lower rate while the secondary output power increases proportionally to the acceleration PSD for $S_a > 3.1 \times 10^{-4}$ g^2 Hz^{-1}. At $S_a = 10.3 \times 10^{-4}$ g^2 Hz^{-1} the secondary output power is comparable to the primary output power. It is about twice the primary power at $S_a = 16.7 \times 10^{-4}$ g^2 Hz^{-1}.

The measured output power of the primary transducers under various acceleration PSDs, S_a, at a bias voltage $V_b = 12$ V are shown in figure 7. At $S_a = 0.9 \times 10^{-5}$ g^2 Hz^{-1}, the primary mass infrequently hits the end-stops. The primary transducers perform linearly at small levels of S_a, giving a maximum peak of the output PSD at a resonance frequency $f_0 = 637.6$ Hz with a 3 dB-bandwidth of 8.9 Hz. Large S_a leads to the primary mass impacting the secondary mass. Then the primary transducers behave nonlinearly. Similar to devices with rigid end-stops, the displacement limitation of the primary mass by the secondary structures makes the primary structure behave as a stiffening-spring device [30, 32–34]. The resonance frequency of the primary transducer is shifted to higher frequencies and the corresponding 3 dB-bandwidth also increases with increasing S_a. For example, a resonance frequency of $f_0 = 649.7$ Hz and a 3 dB-bandwidth of 21.1 Hz

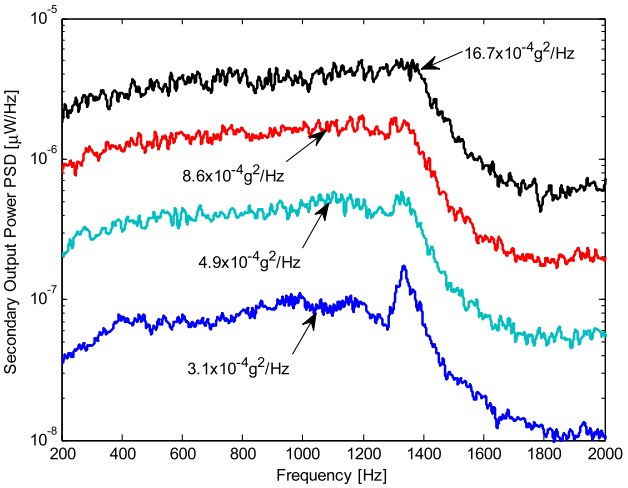

Figure 8. Measured PSDs of the secondary outputs for acceleration PSDs: 3.1×10^{-4} , 4.9×10^{-4}, 8.6×10^{-4} and 16.7×10^{-4} g^2 Hz^{-1} as shown at a bias voltage $V_b = 12$ V.

are the results for $S_a = 3.1 \times 10^{-4}$ g^2 Hz^{-1}. For $S_a = 16.7 \times 10^{-4}$ g^2 Hz^{-1}, the resonance frequency is increased to $f_0 = 677.0$ Hz and the 3 dB-bandwidth is enlarged to 60.4 Hz. This indicates that the 3 dB-bandwidth is increased by a factor of 6.7 when increasing the PSD from $S_a = 0.9 \times 10^{-5}$ to 16.7×10^{-4} g^2 Hz^{-1}.

Figure 8 shows the measured output PSDs of the secondary transducers for different S_a. At low S_a, we already saw in figure 6 that the secondary output power is negligible due to little or no activation from impacts of the primary mass. When reaching $S_a = 3.1 \times 10^{-4}$ g^2 Hz^{-1}, the effect of impacts are noticeable in figure 8 as a peak in the secondary-structure spectrum at about twice the resonant frequency of the primary transducer. When increasing from $S_a = 3.1 \times 10^{-4}$ to 16.7×10^{-4} g^2 Hz^{-1}, the frequent internal impacts between the two structures lead to a substantial increase of the secondary output PSDs. The output PSD of the secondary transducers rises considerably on the low frequency side of the response.

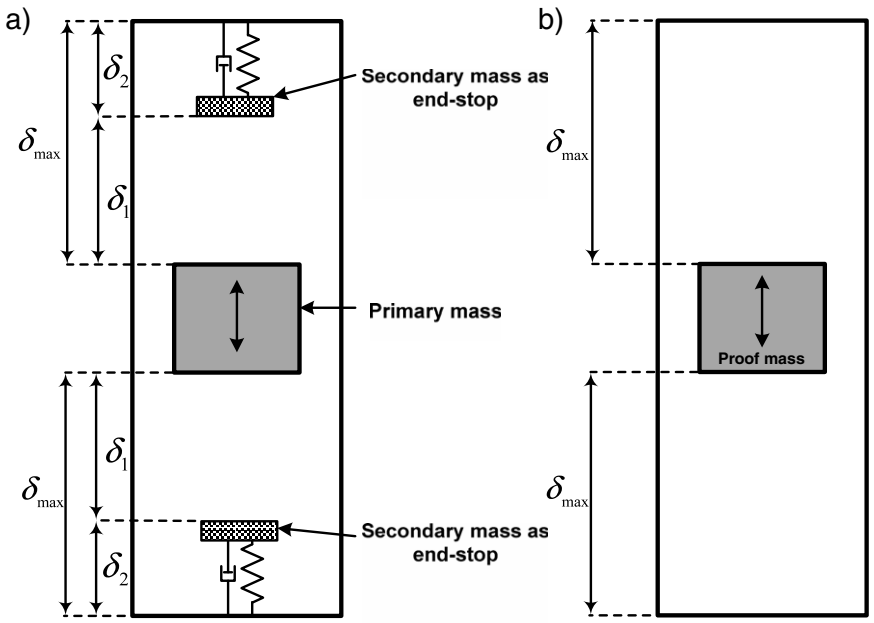

Figure 9. A schematic illustration of comparison between the impact and reference devices: (a) an impact device with two-stage transduction using the end-stops designed as secondary transducers and (b) a reference device with rigid end-stops. Proof mass motion of both devices is limited by a maximum displacement amplitude δ_{max}.

For example, at $S_a = 16.7 \times 10^{-4}$ g^2 Hz^{-1}, the frequency response of the secondary transducer is approximately flat from $f = 200$ Hz to $f = 2f_0 = 1354$ Hz. The output of the secondary transducers is mainly driven by the motion of the primary mass through the internal impact force to the secondary mass.

4. Comparison with reference device performance

Further evaluation of the device concept under wideband excitations is carried out through a comparison with a reference device as illustrated in figure 9. The reference device is designed in the same manner as the primary structure, including a big proof mass and two overlap-varying transducers. The device is identical in design to the one characterized in [18, 30], but is a different sample from the batch for the present investigation. The proof mass has the same die dimension and the same maximum displacement amplitude $\delta_{max} = 10\ \mu$m as the impact device. In the reference design, ordinary rigid end-stops are used to confine the proof mass motion. Due to the omission of secondary transducers, the reference device has a somewhat bigger proof mass and more capacitor fingers in the transducers. In addition, the mechanical quality factors Q_m of the primary and reference transducers are 160 and 205 respectively, based on their impedance characterization. Therefore, the output power of the reference device is higher than that of the impact device at low excitation levels. The load value of the reference transducers is determined as described in section 3.1, giving $R_{Lr} = 14.8$ MΩ. The nominal capacitance is 1.3 pF and the proof mass is 1.2 mg for the reference device, as compared to 1.17 pF and 1.1 mg for the primary transducers of the

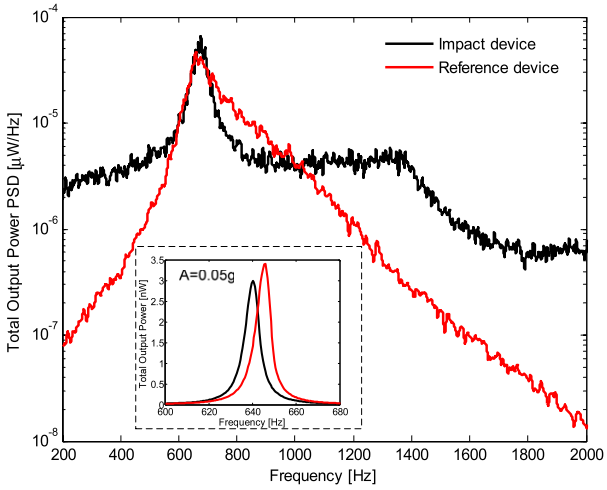

Figure 10. Comparison between measured total output PSDs of the impact and reference devices for $S_a = 16.7 \times 10^{-4}$ g^2 Hz^{-1} at a bias voltage $V_b = 12$ V. Subfigure shows frequency responses of both devices for $A = 0.05$ g harmonic vibration.

impact device. For example, at $A = 0.05$ g, as shown in a subfigure in figure 10, the maximum output powers are 3 nW and 3.4 nW respectively for the impact and reference devices at their resonance frequencies. The suspending springs were adjusted in width to achieve the same nominal resonance frequency. However, due to variant over-etching during device fabrication, their measured resonance frequencies differ by 1.3%. The resonance of the reference device is $f_0 = 645.8$ Hz and the impact device has $f_0 = 637.6$ Hz.

Figure 10 shows a comparison between the measured total output PSDs of the impact and reference devices at

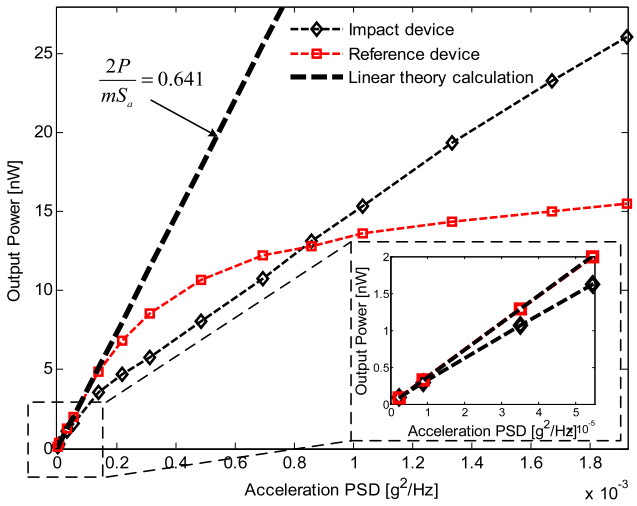

Figure 11. Comparison of total output powers between the impact and reference devices under increased acceleration PSDs at a bias voltage $V_b = 12$ V.

an acceleration PSD of $S_a = 16.7 \times 10^{-4}$ g^2 Hz^{-1}. The contribution of the secondary output PSDs leads to the total output PSD of the impact device being generally higher than that of the reference device in the low and high frequency regions. The internal impact between the secondary and primary masses shifts the resonance frequency of the impact device from 637.6 to 677.0 Hz, higher than that of the reference device 663.8 Hz due to the stiffening effects. For both devices, the response bandwidth of the total output power is also increased by the internal impacts. Around the resonance frequency of the impact device, the total output PSD is roughly that of the primary transducer at a small acceleration PSD. The measured 3 dB bandwidths are 60.4 Hz and 88.6 Hz respectively for the impact and reference devices. The resonance peak of the output PSD for the impact device is 6.5×10^{-5} μW Hz^{-1}, higher than that of reference device of 4.6×10^{-5} μW Hz^{-1}.

Figure 11 shows a comparison of the measured output power of the two devices under increased acceleration PSDs at a bias voltage of $V_b = 12$ V. At low levels of the acceleration PSDs, the total output power of the reference device is higher than that of the impact device since most of the output power of the impact device is obtained from the primary transducers. When the proof mass hits the end-stops, the reference output slowly increases and then exhibits saturation for increasing S_a. The extra harvested power from the impacts on the transducing end-stops causes the total output power of the impact device to continuously increase, instead of saturating as the power does for the reference device with conventional end-stops. The total output power 12.9 nW of the impact device is comparable to that of the reference device at an acceleration PSD $S_a = 8.6 \times 10^{-4}$ g^2 Hz^{-1}. For $S_a = 19.2 \times 10^{-4}$ g^2 Hz^{-1} the total output power is increased up to 26.1 nW for the impact device, while the output power of the reference device is 15.4 nW.

The output powers of both reference and primary transducers are linearly proportional to the input acceleration

Table 2. Reference device parameters.

Parameters	Value
Proof mass, m (mg)	1.2
Spring stiffness, k_m (N m^{-1})	19.2
Damping constant, b (N s m^{-1})	2.37×10^{-5}
Nominal capacitance, C_0 (pF)	1.3
Parasitic capacitance, C_p (pF)	7.5
Parasitic load capacitance, C_L (pF)	5.0
External load, R_{Lr} (MΩ)	14.8
Total electromechanical coupling factor, k^2 (%)	1.8

PSDs for low excitation levels. The output power in this linear regime is given by

$$P = \frac{mS_a}{2} \frac{r_L k^2 Q_m}{1 + (1/Q_m + k^2 Q_m) r_L + r_L^2} \quad (1)$$

where r_L is the normalized load resistance, Q_m is the open-circuit mechanical quality factor and k^2 is the electromechanical coupling factor [35]. The coupling factor can be determined in the linear regime by decoupling the common and differential mode behavior, since the reference device consists of two anti-phase electrostatic transducers. The relevant parameters can be written as [18, 37]

$$k^2 = \frac{2C_0^2 V_b^2}{x_0^2 (C_0 + C_p + C_L) k_m + 2C_0^2 V_b^2}, \quad (2)$$

$$r_L = R_L (C_0 + C_p + C_L) \sqrt{\frac{K}{m}}, \quad (3)$$

$$K = k_m + \frac{2C_0^2 V_b^2}{x_0^2 (C_0 + Cp + C_L)} \quad (4)$$

where x_0 is the nominal overlap of capacitors, k_m is the spring stiffness, C_0 is the nominal capacitance, C_p is a parasitic capacitance in parallel with the variable capacitance and C_L is a parasitic capacitance in parallel with the external loads R_L.

The output power of the reference device is considered as a comparison source to observe the power enhancement of the impact device concept. Therefore, the reference device is characterized in full detail using an LTSPICE simulation model. All model parameters are found by fitting the model to the experimental results in the linear regime and are given in table 2. With the input power $P_{in} = mS_a/2$ [36, 38], the measured efficiency of both devices is estimated by the quantity $\eta = 2P/mS_a$ and the linear theory calculation (1) shows the efficiency of the reference device under the wideband excitations to be

$$\eta = \frac{r_L k^2 Q_m}{1 + (1/Q_m + k^2 Q_m) r_L + r_L^2}. \quad (5)$$

In the linear regime with low levels of the acceleration PSDs, the efficiency of the reference device is 64.1%. The linear theory calculation agrees with the experimental results for the reference device, as shown in the inset in figure 11. The efficiency of the reference device is significantly reduced in the nonlinear regime when the acceleration PSDs are

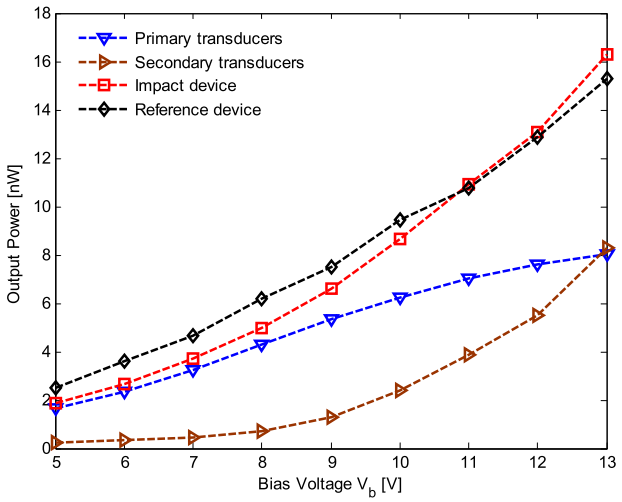

Figure 12. Measured output powers of the impact and reference devices under increased bias voltage V_b at $S_a = 8.6 \times 10^{-4}$ g^2 Hz^{-1}.

sufficiently large to drive the proof mass to impact the end-stops frequently. The practical motion limit considerably reduces further increase of the output power in the reference device performance. For example, the efficiency is decreased from 64.1% down to 14.1% for $S_a = 19.2 \times 10^{-4}$ g^2 Hz^{-1}. However, at this acceleration PSD level, the efficiency of the impact device is 23.6%, which is about 9.5% higher than that of the reference device efficiency. This demonstrates that the two-stage device principle with extra power extracted from the end-stops improves the efficiency compared to the reference device with the same device dimension and the same maximum displacement amplitude δ_{max}.

Figure 12 shows the effects of the bias voltage V_b on the outputs at $S_a = 8.6 \times 10^{-4}$ g^2 Hz^{-1} where the powers of the impact and reference devices become approximately equal, see figure 11. For the impact device, the obtained power of the primary transducers increases with the bias V_b, but high bias-values are required to obtain significant benefits from the gap-closing transducers of the end-stops. The output power will be quadratic in V_b at a given displacement amplitude for all the transducers types. The gap-closing transducers of the end-stops differ from the overlap-varying primary and reference transducers in displaying electromechanical softening, as opposed to stiffening, with increasing bias. In addition, the gap-closing transducers are particularly ineffective at small displacements, due to small capacitance changes, and therefore benefit from the larger displacements made possible by their lowered stiffness at higher bias. The output power of the secondary transducers becomes equal to that of the primary transducers at $V_b = 13$ V. Comparing to the reference device, the total output power of the impact device is less for $V_b \leq 10$ V due to the small contribution of the secondary structures. The impact device gives comparable and higher output power than that of the reference device for only $V_b \geq 11$ V.

As shown in the sketch in figure 3, both the primary and secondary transducers are biased by the same voltage in our experiments. The admissible bias for the secondary transducers, even though they are symmetric, is limited by pull-in. From the design parameters, we estimated the static pull-in voltage to be $V_{pull\text{-}in} = 20.1$ V without inclusion of parasitic capacitance effects. This point motivates further investigations on an experimentally more complicated configuration with separate biases for the primary and secondary transducers, permitting independent optimization for the two types of transducers.

The results of the device comparison show that the impact device requires a certain acceleration level to activate the secondary transducers effectively to give an advantage, as is the case beyond $S_a = 8.6 \times 10^{-4}$ g^2 Hz^{-1} in figure 11. This can be attributed to the secondary structures being rather stiff and their gap-closing transducers being insensitive to small changes of their nominal gap. To reduce this 'acceleration gap' in future work, it is therefore of interest to investigate more compliant secondary structures and also to investigate methods to make the end-stop transducer more sensitive to small electrode displacement. Such optimization of the transducing end-stops would make the device efficiency even closer to the linear-regime value under displacement limited operation.

5. Conclusion

The utilization of end-stops as additional secondary transducers has been investigated by design of a two-stage impact device and by its characterization under wideband vibrations. A sufficiently strong ambient vibration drives the primary proof mass to its maximum displacement, allowing additional power to be obtained from the internal impacts. This secondary power can be comparable to the primary output power in this device design. The extra contribution from the transducing end-stops gives higher output powers and enhanced performance efficiency in comparison with use of ordinary end-stops constraining the proof mass motion. As an extra feature, the nonlinearity of the impact mechanism increases the response bandwidth of the impact device.

Acknowledgment

This work was supported by the Research Council of Norway under Grant no. 191282.

References

[1] Williams C B and Yates R B 1996 Analysis of a micro-electric generator for microsystems *J. Sensors Actuators* A **52** 8–11
[2] Roundy S, Wright P K and Rabaey J 2003 A study of low level vibrations as a power source for wireless sensor nodes *Comput. Commun.* **26** 1131–44
[3] Cantatore E and Ouwerkerk M 2006 Energy scavenging and power management in networks of autonomous microsensors *Microelectron. J.* **37** 1584–90
[4] Beeby S P, Tudor M J and White N M 2006 Energy harvesting vibration sources for microsystems applications *J. Meas. Sci. Technol.* **17** 175–95
[5] Mitcheson P D, Yeatman E M, Rao G K, Holmes A S and Green T C 2008 Energy harvesting from human and machine motion for wireless electronic devices *Proc. IEEE* **96** 1457–86

[6] Roundy S, Wright P K and Rabaey J M 2004 *Energy Scavenging for Wireless Sensor Networks with Special Focus on Vibrations* (Dordrecht: Kluwer Academic)

[7] Anton S R and Sodano H A 2007 A review of power harvesting using piezoelectric materials (2003–2006) *Smart Mater. Struct.* **16** R1–21

[8] Starner T 1996 Human-powered wearable computing *IBM Syst. J.* **35** 618–29

[9] Moll F and Rubio A 2000 An approach to the analysis of wearable body-powered systems *Proc. Mixed Design of Integrated Circuits and Systems Conf. (Gdynia, June)*

[10] Tvedt L G W, Blystad L-C J and Halvorsen E 2008 Simulation of an electrostatic energy harvester at large amplitude narrow and wide band vibrations *Proc. Symp. Design, Test, Integration and Packaging of MEMS/MOEMS-DTIP2008 (Nice, April)* pp 296–301

[11] Soliman M S M, Abdel-Rahman E M, El-Saadany E F and Mansour R R 2008 A wideband vibration-based energy harvester *J. Miromech. Microeng.* **18** 115021

[12] Hoffmann D, Folkmer B and Manoli Y 2009 Fabrication, characterization and modelling of electrostatic miro-generators *J. Miromech. Miroeng.* **19** 094001

[13] Blystad L-C J and Halvorsen E 2010 A piezoelectric energy harvester with a mechanical end stop on one side *Proc. Symp. Design, Test, Integration and Packaging of MEMS/MOEMS-DTIP2010 (Seville, May)* pp 259–62

[14] Blystad L-C J and Halvorsen E 2011 A piezoelectric energy harvester with a mechanical end stop on one side *J. Microsyst. Technol.* **17** 505–11

[15] Blystad L-C J, Halvorsen E and Husa S 2010 Piezoelectric MEMS energy harvesting systems driven by harmonic and random vibrations *IEEE Trans. Ultrason. Ferroelectr. Freq. Control* **57** 908–19

[16] Le C P and Halvorsen E 2009 Evaluation of parameters for electrostatic energy harvesters *Proc. Symp. Design, Test, Integration and Packaging of MEMS/MOEMS-DTIP2009 (Rome, April)* pp 286–91

[17] Liu H, Tay C J, Quan C, Kobayashi T and Lee C 2011 Piezoelectric MEMS energy harvester for low-frequency vibrations with wideband operation range and steadily increased output power *J. Microelectromech. Syst.* **20** 1131–42

[18] Le C P and Halvorsen E 2012 MEMS electrostatic energy harvesters with end-stop effects *J. Miromech. Microeng.* **22** 074013

[19] Umeda M, Nakamura K and Ueha S 1996 Analysis of the transformation of mechanical impact energy to electric energy using piezoelectric vibrator *Japan. J. Appl. Phys.* **35** 3267–73

[20] Umeda M, Nakamura K and Ueha S 1997 Energy storage characteristics of a piezo-generator using impact induced vibration *Japan. J. Appl. Phys.* **36** 3146–51

[21] Xu C N, Akiyama M, Nonaka K and Watanabe T 1998 Electrical power generation characteristics of PZT piezoelectric ceramics *IEEE Trans. Ultrason. Ferroelectr. Freq. Control* **45** 1065–70

[22] Funasaka T, Furuhata M, Hashimoto Y and Nakamura K 1998 Piezoelectric generator using a $LiNbO_3$ plate with an inverted domain *Proc. Int. IEEE Ultra. Symp. (Sendai, Oct.)* pp 959–62

[23] Yoon S H, Lee Y H, Lee S W and Lee C 2008 Energy-harvesting characteristics of PZT-5A under gunfire shock *Mater. Lett.* **62** 3632–5

[24] Djugum R, Trivailo P and Graves K 2009 A study of energy harvesting from piezoelectrics using impact forces *Eur. Phys. J. Appl. Phys.* **48** 11101

[25] Gu L 2011 Low-frequency piezoelectric energy harvesting prototype suitable for the MEMS implementation *Microelectron. J.* **42** 277–82

[26] Rastegar J, Pereira C and Nguyen H L 2006 Piezoelectric-based power sources for harvesting energy from platforms with low frequency vibration *Proc. SPIE* **6171** 617101

[27] Moss S 2011 Vibration energy conversion device *US Provisional Patent* 61/482 496

[28] Moss S, Barry A, Powlesland I, Galea S and Carman G P 2011 A broadband vibro-impacting power harvester with symmetrical piezoelectric bimorph-stops *Smart Mater. Struct.* **20** 045013

[29] Moss S, McLeod J and Galea S 2012 Wideband vibro-impacting vibration energy harvesting using magnetoelectric transduction *J. Int. Mater. Syst. Struct.* doi:10.1177/1045389X12443598

[30] Le C P, Halvorsen E, Søråsen O and Yeatman E M 2012 Microscale electrostatic energy harvester using internal impacts *J. Int. Mater. Syst. Struct.* **23** 1409–21

[31] www.memscap.com/products/mumps/soimumps

[32] Mestrom R M C, Fey R H B, Phan K L and Nijmeijer H 2010 Simulations and experiments of hardening and softening resonances in a clamped–clamped beam MEMS resonator *Sensors Actuators* A **162** 225–34

[33] Elshurafa A M, Khirallah K, Tawfik H H, Emira A, Aziz A K S A and Sedky S M 2011 Nonlinear dynamics of spring softening and hardening in folded-MEMS comb drive resonators *J. Microelectromech. Syst.* **20** 943–58

[34] Ashraf K, Khir M H Md, Dennis J O and Baharudin Z 2013 A wideband, frequency up-converting bounded vibration energy harvester for a low-frequency environment *Smart Mater. Struct.* **22** 025018

[35] Halvorsen E 2008 Energy harvesters driven by broadband random vibrations *J. Microelectromech. Syst.* **17** 1061–71

[36] Scruggs J T 2009 An optimal stochastic control theory for distributed energy harvesting networks *J. Sound Vib.* **320** 707–25

[37] D'hulst R, Sterken T, Fiorini P, Puers R and Driesen J 2007 Energy scavengers: modeling and behavior with different load circuits *Proc. 33rd Annual Conf. IEEE Industrial Electronics Society (IECON) (Taipei, Nov. 2007)* pp 2169–74

[38] Halvorsen E 2013 Fundamental issues in nonlinear wide-band vibration energy harvesting *Phys. Rev.* E **87** 042129